Imaging Plasmon Hybridization of Fano Resonances *via* Hot-Electron-Mediated Absorption Mapping

Sabrina Simoncelli,[1‡]* Yi Li,[1‡] Emiliano Cortés,[1]* Stefan A. Maier[12]

[1]The Blackett Laboratory, Department of Physics, Imperial College London, London SW7 2AZ, United Kingdom.

[2]Chair in Hybrid Nanosystems, Faculty of Physics, Ludwig-Maximilians-Universität München, 80799 München, Germany.

* E-mail: s.simoncelli@imperial.ac.uk, e.cortes@imperial.ac.uk

ABSTRACT.

The inhibition of radiative losses in dark plasmon modes allows storing electromagnetic energy more efficiently than in far field excitable bright-plasmon modes. As such, processes benefiting from the enhanced absorption of light in plasmonic materials could also take profit of dark plasmon modes to boost and control nanoscale energy collection, storage and transfer. We experimentally probe this process by imaging - with nanoscale precision - the hot-electron driven desorption of thiolated molecules from the surface of gold Fano nanostructures, investigating the effect of wavelength and polarization of the incident light. Spatially-resolved absorption maps allow us to show the contribution of each element of the

nanoantenna in the hot-electron driven process and their interplay in exciting a dark plasmon mode. Plasmon-mode engineering allows control of nanoscale reactivity and offers a route to further enhance and manipulate hot-electron driven chemical reactions and energy-conversion and transfer at the nanoscale.

Progress in controlling and tuning light-matter interactions has expanded our ability to collect, store and convert energy at the nanoscale. Plasmonic materials have played a crucial role in enhancing such interactions due to localized surface plasmon resonances (LSPRs) that can be excited after light impinges on a metal nanoparticle (NP).[1] The incident electric field – of a given frequency – drives the conduction electrons of the NP in collective oscillations, known as LSPRs. The interaction with light is so intense that the typical extinction cross section of a metal NP illuminated at its LSPR is more than ten times larger than its geometrical size.[2] This incident energy can be partially scattered to the far field and partially absorbed by the NP, providing kinetic energy to its conduction electrons. Both of these processes have found interesting applications, either using the NPs as antennas to couple the near- and far-fields or by the multiple uses of the kinetic energy storage in the free electrons movement.[3] The relaxation of this last phenomena triggers a series of processes such as the generation of energetic (hot) electron-hole pairs,[4] propagation of lattice phonons[5] and nanoscale heating,[6] among others.[7] These effects have turned metal NPs into key players in the manipulation of light at the nanoscale.

One of the many parameters that can be tuned in order to control light-matter interactions in plasmonic systems is the type of plasmon modes that can be excited in

the metal NP.[8] When illuminated from the far field at normal incident angle, only plasmon modes of odd mode parity (*i.e.* bright modes) can be excited.[9] These modes highly efficiently re-radiate/collect energy from the near to the far field or *vice-versa* and as such, most of the applications of the metal NPs as nanoantennas have benefit from them. However, for those applications where the absorption of light needs to be enhanced, plasmon modes with even parity (*i.e.* dark modes) could be more beneficial. These modes by virtue of having vanishing dipole moments can store electromagnetic energy more efficiently than modes with dipolar character (bright modes) due to inhibition of radiative losses.[10] Dark plasmon modes can be activated either through highly angled illumination or by coupling to a dipolar resonance with symmetry breaking owing to their faint dipole moment.[11-14] In this last scenario, a bright element is needed in order to couple the light from the far field and then – under given conditions – transfers it into the dark element. This plasmon hybridization process is characterized by the appearance of a sharp and asymmetric peak in the plasmon response of the system, typical of Fano-type interference processes.[15]

Fano resonances in plasmonic systems have been widely explored in recent years.[14,16,17] Briefly, the broad plasmon resonance of bright modes acts as a continuum of states that hybridize with discrete states such as a dark plasmon mode,[18,19] the electronic excitation of a molecule,[20,21] the excitation of a diffraction channel[15,22-24] or a guided mode,[25] amongst others.[26] As a consequence, narrow spectral lines appear in the spectra of these systems, *aka* Fano resonances, attaining many applications such as enhanced sensing capabilities,[27] high-Q optical cavities, near field imaging methods,[28] lossless waveguides, *etc*. Recent advances in channelling, storage and conversion of electromagnetic energy at the nanoscale[29] –

like hot-electron driven chemical reactions – can also benefit from a deeper understanding and exploitation of this type of resonances.[30,31] In the particular case of a dark plasmon mode overlapping with a broad bright plasmon mode, the far field scattering is minimum at the Fano resonance frequency while the absorption is maximized.[32–34] This should in turn lead to an enhancement of hot-electron production,[35] being them localized in the dark element of the plasmonic system; also offering exciting opportunities for controlling energy flow and reactivity at the nanoscale. However, access to this spatially-resolved information is not trivial.[36] Dark plasmon modes do not radiate to the far field, thus imaging them using conventional optical techniques is not possible.[37] Near field techniques, however, have proven more suitable for spatially resolving the plasmon modes phase and intensity in these highly coupled systems.[38]

In this letter we demonstrate hot-electron Au-S cleavage driven by a dark plasmon mode at the frequency of a Fano resonance. Hot electrons excited upon plasmon decay in Au nanostructures lead to thiol desorption (see Figure 1a), which also serves as a super-resolution imaging method *via* m-PAINT.[39] By using this recently developed super-resolution fluorescence microscopy approach, we were able to image the wavelength-dependent reactivity of each element of a Fano-type nanonantenna, thus also providing a spatially-resolved (sub-diffraction) absorption map of a highly coupled plasmonic system that possess a Fano resonance (see Figure 1b). Imaging dark plasmon modes *via* their hot-electron generation as well as revealing the interplay between components of the plasmonic system *via* their local reactivity is key to examine unexplored paths for efficient hot-electron production, manipulation and transfer.

The demonstration of our Fano nanosystem begins with a gold nanorod of 340 nm in length and 85 nm in width as depicted in Figure 2a, which in principle holds an $l = 2$ resonance in the wavelength range of interest (*i.e.* 600-1000 nm). Since this even parity mode can only be accessed with a broken symmetry, numerical calculations for both normal ($\theta = 0°$) and $\theta = 16°$ incidence angles are shown in Figure 2a (bottom) when the light is polarised perpendicular to the shorter axis of the nanorod. We can observe a resonant peak belonging to the designed mode at 16° incidence angle. To further understand this peak, the charge distributions for the lowest three modes of this nanorod are displayed in Figure 2a (top). The mode at this wavelength, 860 nm ($l = 2$), has one polarity of charges at both terminals of the rod, while the other polarity concentrates nearly at the centre; typical of a dark-mode. The combination of far field spectra and near field distribution are in line with our expectations from mode parity theory.[9] To activate this $l = 2$ mode with normal incidence light, we design gold nanodisks of 160 nm diameter that present a relative broad dipolar resonance centre at 810 nm wavelength, represented by the dashed grey area in Figure 2a.

The coupling of the two disks and the rod with a gap size of ~20 nm as an individual cluster leads to a typical Fano interference in the far field spectra. This can be noticed in the measured and simulated scattering spectra of this cluster in air as presented in Figure 2b, where a dip appears on the scattering spectrum at around 780 nm. Note that this plasmon hybridization between the bar and the disks can only occur when illuminating the structure with parallel polarization (along the gap between the bar and the disks), while it disappears when rotating the polarization by 90° (see Figure S1). To further analyse the operation of this Fano cluster, the charge distributions (in water) for both incident polarizations are shown in Figure 3. The Fano interference forms when the incident light is polarised parallel to the gaps,

where the energy can couple into the $l = 2$ dark mode *via* the electromagnetic enhancement in the near field (see Figure 3b, 935 nm, top). In this way, the dark mode can be efficiently excited and due to their vanished radiative properties and enhanced absorption this should lead to the generation of hot-carriers in the dark element of the structure.

The corresponding calculated absorption spectra and resistive losses maps for this Fano cluster in water are summarized in Figure 3. Three different wavelengths, at 750 nm, 820 nm and 935 nm are illustrated. For the case of parallel polarization (parallel polarization corresponds to the electrical field polarized along the gap direction in the Fano structure) the main results can be summarized as follows: a) when the cluster operates off resonance, the optical absorption is fairly limited and concentrated in the disks, as reflected in the resistive losses maps; b) at the peak of the scattering spectra, the bright mode of the disks dominate and while the absorption is highly confined in the disks, the bar also starts to slightly absorb the near field light, and c) at the peak of absorption, 935 nm, which is close to the dip of the scattering spectrum, the absorption in the bar is much higher than the absorption in the two disks, which implies that a strong dissipation of hot electrons could occur in the bar compared with the disks. Note that for perpendicular polarization (Figure 3 bottom) the dark mode cannot be excited in the range of wavelengths investigated here. This is in agreement with the polarization-dependence of our Fano cluster, as shown in Figures 2b and S1.

Now that we have identified the spectral behaviour of our Fano structure as well as calculated the local absorption of each sub-element of the antenna (*i.e.* resistive losses in the disks and the bar), we turn to designing the experiments that will allow us to access to this information. In order to map the spatial distribution of

6

absorption in our Fano cluster we use a hot-electron induced desorption reaction, as shown in Figure 1. We have recently demonstrated that this reaction can be used as a reporter of the resistive losses in plasmonic structures.[39] To trigger the reaction we illuminate the nanostructures with a femtosecond laser, tuned at different wavelengths and polarizations, as described in detail in the next sections. After that, we image the already irradiated structures by using a super-resolution technique. This last step allows us to identify the regions where the molecular desorption has taken place within the structure (*i.e.* where the hot-electron induced reaction was activated).

To experimentally acquire the density absorption maps of the disks and the bar in the Fano structure we use metallic DNA-PAINT (m-PAINT).[39] m-PAINT is a single-molecule based super-resolution imaging techniques that allows us to map the positions of thiol-gold bonds on the surface of nanostructures with nanoscale precision. The basic principle of this technique is to induce stochastic fluorescent events by taking advantage of the binding kinetics between fluorescently labelled single-stranded DNA molecules freely diffusing in solution (imager strands) and DNA oligonucleotides chemically anchored to metal surfaces through a gold-thiol bond (docking strands) (Figure 4a). Thus, when an imager strand binds to a docking strand a fluorescent signal appears as a diffraction-limited spot on the object. In this way, transient binding can only happen when a docking strand is found on the surface by the imager strand. This transient binding is destroyed when the imager strand dehybridizes.

For m-PAINT measurements, we use a custom-built total internal reflection fluorescence microscope set-up. For all the super-resolution images in this letter we used a 647 nm linearly polarized light at an excitation intensity of ~ 850 W cm^{-2}, in order to excite the fluorescent probes. Imager strands were fluorescently labeled with

Atto655, whose absorption and emission spectra are largely off the Fano resonance mode of the plasmonic antenna, however, not completely decoupled to the higher radiative modes of the structure.[40] Super-resolution images were reconstructed from the raw data (40,000 frames, frame rate 33Hz) using in-house MATLAB routines. More details on the experimental details (DNA functionalization, optical microscopy and super-resolution data processing and image analysis) can be found in Sections S4 to S6 of the Supporting Information.

Figure 4b and Figure S2 show typical super-resolved images of individual gold Fano nanostructures of dimensions 340×80 nm^2 (bar) and 160 nm (disks, diameter) obtained with m-PAINT with optimized imaging conditions (*e.g.*, density of docking strands, concentration of imager strands, number of frames, laser excitation power, *etc.*). With our imaging configuration, we achieved an average localization precision of 24 nm enabling us to clearly resolve gold-thiol bonds located either in the disks or in the bar of the Fano structure (see Figure S3 in the Supporting Information). Next, we generated an "average" super-resolution image (Figure 4d) by summing the single-molecule localizations of 36 individual Fano structures using a translation registration algorithm to align their centre of mass (see Section 6 of the Supporting Information). The average image is in reasonably good agreement with the dimensions and geometry of the fabricated Fano structures as evidenced by the similarity between the super-resolution (Figure 4d) and SEM (Figure 4c) images. The main differences are observed in the bar, as it looks dimmer than the disks in the m-PAINT image, thus, suggesting a moderate coupling effect[40–44] between the antenna and the fluorophore as detailed in Section 8 and Figure S4 of the Supporting Information.

As already mentioned, one potential advantage of m-PAINT when combined with femtosecond illumination is its ability to experimentally image the resistive losses distribution (or its complement) of single antennas at different excitation wavelengths, which spans beyond typical near field imaging approaches of plasmonic properties. Previous studies of photo-release of thiolated DNA molecules from gold nanostructures have shown that under pulsed illumination DNA is released by inducing gold-thiol bond cleavage through a plasmon-induced charge transfer mechanism.[39,45,46] Here, we take advantage of this fact in order to map hot-electron spatial distribution under different illumination conditions by imaging the gold-thiol bonds that remain on the Fano structure after femtosecond illumination. To irradiate individual nanostructures at different wavelengths and polarization directions we employ an optical microscope coupled to a linearly polarized femtosecond pulsed laser source and equipped with a nanopositioning piezo-stage, which allows irradiating micro-sized arrays in just a few seconds (see Section 7 of the Supporting Information). After the femtosecond irradiation step is completed, we image the remaining docking strands in the Fano nanostructures using m-PAINT. Figure 5 (middle row) shows the average super-resolution images of ∼ 32 to 35 individual Fano nanostructures when varying the polarization and excitation wavelength of the pulsed-illumination. In agreement with Halas and co-workers,[45] we have recently shown that under these experimental conditions, the hot-electron route can be identified as the main mechanism behind thiol-desorption from plasmonic structures under femtosecond illumination conditions.[39]

Noticeably, in all cases, the m-PAINT images suitably reproduce their corresponding numerically calculated maps (Figure 5, bottom row). To build up the calculated maps two major effects have been considered: i) the resistive losses of the

structure, P_{loss}, evaluated at the illumination wavelength and experimental fluence of the ultrafast laser, and ii) the coupling effect between the dye and the antenna during the super-resolution imaging, $(\gamma/\gamma^0)_{exc}(\phi/\phi^0)_f$. Regarding the first point, it should be noted that hot-electron spatial-reactivity relies on both the energy and the density of the generated hot electrons.[47] In our experiments, the energy range - set by the excitation wavelengths (~1.3 to ~1.6 eV) - matches the energy range of unoccupied Au–S states (~1.2 to ~1.4 eV above the Fermi level).[48,49] On the other hand, the density of electrons is given by the resistive losses of the structure, meaning that regions with higher resistive losses will be more reactive – if they have enough energy to react - as it has been recently shown.[39,50] In the particular case of thiol desorption, resistive losses scale linearly with the fs irradiation fluence,[39] implying that different super-resolution absorption maps can be obtained depending on the fluence of the femtosecond laser irradiation (see for example Figure S6). For the images shown in Figure 5 (middle row), we kept the fluence of the ultrafast laser nearly constant for all the different wavelengths investigated here. The obtained trends demostrate that the changes observed here derive from the magnitude and distribution of the resistive losses – *i.e.* absorption - within the structure, more than the fluence of the laser. For a given fluence, the anisotropic distribution of resistive losses in the Fano structure results in an on-set value above which thiol-desorption events are observable (*i.e.* it is required enough density of carriers to start desorbing the molecules). To set this threshold of resistive losses, P_{loss}^{thres}, we tested different values and kept the one that best described the experimental data set of Figure 5.

The second effect that we considered in order to build up the calculated maps in Figure 5 is the coupling between the fluorescent dye and the antenna, usually referred in the literature as "mislocalization". In our experiments, the dye-antenna

10

coupling effect is the same for all these cases (see Figure S4), as the imaging conditions are always the same (λ_{exc}= 647 nm laser, dye Atto655 and the same Au antenna pre-irradiated at different wavelengths). As such, the differences observed in Figure 5 cannot arise from a coupling (mislocalization) effect. On the contrary, the calculated maps are in a reasonable agreement with the fact that gold-thiol cleavage is a hot-electron induced process and that these energetic electrons are localized in regions of dense resistive losses of the structure.[39] Further details on the calculated maps can be found in the supplementary information (Figure S5).

As shown in Figure 5, for parallel polarization, the resistive losses are either localized in the disks (750 nm, violet) or in the bar (935 nm, green, Fano resonance) of the Fano structure, depending if we excite a bright or dark mode, respectively. This is evidenced by the fact that only the thiol-gold bonds localized either in the bar or in the disks of the Fano structure remain after pulsed-illumination with 750 nm and 935 nm, respectively. On the other hand, if we excite the Fano structure with perpendicular polarization, the resistive losses are smaller compared to the parallel case and are mainly localized in the disks independently of the excitation wavelength (for ranges between 750 and 1100 nm), in agreement with Figure 3. This selectivity in DNA spatial release profile from the same DNA–nanostructure complex provides strong evidence of plasmon-induced hybridization in the Fano structure and it can be understood as follows. If we excite our system *via* the broad plasmon resonance of the gold disks, the plasmons of the two gold disks are in resonance and can absorb the far field light, confining the resistive losses of the system in the disks. At the same frequencies, the bar cannot be excited from the far field, as it does not hold any bright plasmon modes in that spectral region. However, illumination with the near field of the disks located in close vicinity to the bar (~ 20 nm, see Figure 3b) can excite the

non-radiative dark mode of the bar, shifting now the resistive losses of the system to the bar. This near field coupling between the two disks and the bar is only active in the case of parallel polarization and here, we show, that it can be exploited to induce hot-electron reactions in an element that intrinsically cannot be excited from the far-field.

Finally, in order to confirm the nature of the Fano-interference process we performed a control experiment by separating the bar and the disks by a larger gap-size (~ 120 nm). By increasing the gap size between the dark and the bright elements of the structure, the hybridization process through near field coupling is greatly reduced. This is reflected in the calculated absorption cross-section of the structure as a function of the gap-size, as shown in Figure 6a. For the range of wavelengths of the Fano-interference in our Dolmen-type structure (850-1000 nm), the hybridization process is fully vanished for a gap size larger than ~ 40 nm (see also the scattering cross-section, Figure S7). As an example, the calculated absorption cross-section of the structure at 935 nm, drops ~ 2.4 times when switching a 20 nm to 120 nm gap-size between the bar and the disks (inset in Figure 6a). This drop in the absorption is a signature of the disappearance of the Fano resonance with increasing the gap size. In order to experimentally corroborate this drop in the absorption maps we fabricated the same Dolmen-type structure shown in Figure 5 but with an increased gap size of ~120 nm between the bar and the disks, as shown in the SEM image in Figure 6b. The m-PAINT super-resolution images of the structure before and after 935 nm ultrafast laser irradiation are also shown in Figure 6c and d, respectively. At this wavelength, we already demonstrated that for a gap of 20 nm only the molecules located in the bar of the structure can be fully desorbed due to the Fano-interference process (Figure 5). However, as shown in Figure 6d, the post-irradiated super-resolution map does not

differ from the original (not-irradiated one), when using the same power and irradiation times as described in Figure 5. These results reflect that molecular desorption cannot take place under these conditions when the gap size is increased up to ~120 nm. This result confirms the expected drop in the absorption cross-section of the structure (inset Figure 6a), and it also matches with the calculated map, considering both the resistive losses of the new structure and the dye-antenna coupling effect (Figure 6e and S4b). This simple example shows how the absorption cross-section of a gold bar can be enhanced more than two times by plasmon hybridization.

In conclusion, we demonstrated the hybridization process taking place in a Fano-type of plasmonic system *via* nanoscale absorption mapping of its constituting elements. Our dolmen-type gold nanoantenna - consisting of a single bar and two disks - show that the absorbed energy can be spatially controlled depending on the excitation wavelength and polarization. Relaying on the hybridization nature of the Fano interference process, the bright mode of the disks and/or the dark mode of the bar can be excited/imaged and, as such, it allows for ultrafast hot electron reactions occurring either on the disks or on the bar-shaped elements. Our advanced experimental method that combines, super-resolution imaging and ultrafast excitation, for the first time provide the unique near field distributions of plasmonic non-radiative hot electron channels at Fano resonances. The insight of energy management through elements paves the way to control the local reactions of the strongly coupled clusters, which will undoubtedly find applications on hot electron generation, control and injection.

ASSOCIATED CONTENT

Supporting Information. The Supporting Information is available free of charge on the ACS Publications website.

Gold nanostructures fabrication, scanning electron microscopy (SEM) imaging, dark field scattering spectroscopy, gold antennas-DNA functionalization, fluorescence microscopy imaging, super-resolution data processing and image analysis, femtosecond pulsed-laser irradiation, numerical simulations, plasmonic response of the Fano structure, super resolution m-PAINT imaging of gold nanostructures, localization precision and cross-sectional histograms, polarized m-PAINT images and calculated total fluorescence enhancements.

AUTHOR INFORMATION

Corresponding Author

*E-mail: s.simoncelli@imperial.ac.uk (S.S.), e.cortes@imperial.ac.uk (E.C.)

Author Contributions

‡These authors contributed equally.

Notes

The authors declare no competing financial interest

References

(1)   Giannini, V.; Fernández-Domínguez, A. I.; Heck, S. C.; Maier, S. A. *Chem. Rev.* **2011**, *111*, 3888–3912.

(2)   Bohren, C. F. *Am. J. Phys.* **1983**, *51*, 323–327.

(3)   Halas, N. J.; Lal, S.; Chang, W. S.; Link, S.; Nordlander, P. *Chem. Rev.* **2011**, *111*, 3913–3961.

(4)   Brongersma, M. L.; Halas, N. J.; Nordlander, P. *Nat. Nanotechnol.* **2015**, *10*, 25–34.

(5)   Della Picca, F.; Berte, R.; Rahmani, M.; Albella, P.; Bujjamer, J. M.; Poblet, M.; Cortés, E.; Maier, S. A.; Bragas, A. *Nano Lett.* **2016**, *16*, 1428–1434.

(6)   Baffou, G.; Quidant, R. *Laser Photonics Rev.* **2013**, *7*, 171–187.

(7)   Khurgin, J. B. *Nat. Nanotechnol.* **2015**, *10*, 2–6.

(8)   Sonnefraud, Y.; Verellen, N.; Sobhani, H.; Vandenbosch, G. A. E. E.; Moshchalkov, V. V.; Van Dorpe, P.; Nordlander, P.; Maier, S. a. *ACS Nano* **2010**, *4*, 1664–1670.

(9)   Verellen, N.; López-Tejeira, F.; Paniagua-Domínguez, R.; Vercruysse, D.; Denkova, D.; Lagae, L.; Van Dorpe, P.; Moshchalkov, V. V.; Sánchez-Gil, J. a. *Nano Lett.* **2014**, *14*, 2322–2329.

(10)   Gómez, D. E.; Teo, Z. Q.; Altissimo, M.; Davis, T. J.; Earl, S.; Roberts, A. *Nano Lett.* **2013**, *13*, 3722–3728.

(11)   Liu, N.; Langguth, L.; Weiss, T.; Kästel, J.; Fleischhauer, M.; Pfau, T.; Giessen, H. *Nat. Mater.* **2009**, *8*, 758–762.

(12)   Maier, S. A. *Nat. Mater.* **2009**, *8*, 699–700.

(13)   Liu, M.; Lee, T. W.; Gray, S. K.; Guyot-Sionnest, P.; Pelton, M. *Phys. Rev. Lett.* **2009**, *102*, 107401.

(14)   Giannini, V.; Francescato, Y.; Amrania, H.; Phillips, C. C.; Maier, S. A. *Nano Lett.* **2011**, *11*, 2835–2840.

(15)   Fano, U. *J. Opt. Soc. Am.* **1941**, *31*, 213.

(16)   Luk'yanchuk, B.; Zheludev, N. I.; Maier, S. A.; Halas, N. J.; Nordlander, P.; Giessen, H.; Chong, C. T. *Nat. Mater.* **2010**, *9*, 707–715.

(17)   Miroshnichenko, A. E.; Flach, S.; Kivshar, Y. S. *Rev. Mod. Phys.* **2010**, *82*, 2257–2298.

(18)   Hao, F.; Sonnefraud, Y.; Van Dorpe, P.; Maier, S. A.; Halas, N. J.; Nordlander, P. *Nano Lett.* **2008**, *8*, 3983–3988.

(19)   Verellen, N.; Sonnefraud, Y.; Sobhani, H.; Hao, F.; Moshehalkov, V. V.; Van Dorpe, P.; Nordlander, P.; Maier, S. A. *Nano Lett.* **2009**, *9*, 1663–1667.

(20)   Pryce, I. M.; Aydin, K.; Kelaita, Y. A.; Briggs, R. M.; Atwater, H. A. *Nano Lett.* **2010**, *10*, 4222–4227.

(21)   Neubrech, F.; Pucci, A.; Cornelius, T. W.; Karim, S.; García-Etxarri, A.; Aizpurua, J. *Phys. Rev. Lett.* **2008**, *101*, 157403.

(22)   Ebbesen, T. W.; Lezec, H. J.; Ghaemi, H. F.; T. Thio; A.Wolff, P.; Thio, T.; A.Wolff, P. *Nature* **1998**, *86*, 1114–1117.

(23)   Auguié, B.; Barnes, W. L. *Phys. Rev. Lett.* **2008**, *101*, 143902.

(24)   Vecchi, G.; Giannini, V.; Gómez Rivas, J. *Phys. Rev. Lett.* **2009**, *102*, 146807.

(25)   Christ, A.; Tikhodeev, S. G.; Gippius, N. A.; Kuhl, J.; Giessen, H. *Phys. Rev. Lett.* **2003**, *91*, 183901.

(26)   Pakizeh, T.; Langhammer, C.; Zorić, I.; Apell, P.; Käll, M. *Nano Lett.* **2009**, *9*, 882–886.

(27)   Liu, N.; Weiss, T.; Mesch, M.; Langguth, L.; Eigenthaler, U.; Hirscher, M.; Sönnichsen, C.; Giessen, H. *Nano Lett.* **2010**, *10*, 1103–1107.

(28)   Caselli, N.; Intonti, F.; La China, F.; Riboli, F.; Gerardino, A.; Bao, W.; Bargioni, A. W.; Li, L.; Linfield, E. H.; Pagliano, F.; Fiore, A.; Gurioli, M. *Light Sci. Appl.* **2015**, *4*, e326.

(29)   Aslam, U.; Chavez, S.; Linic, S. *Nat. Nanotechnol.* **2017**, *12*, 1000–1005.

(30)   Ahmadivand, A.; Sinha, R.; Vabbina, P. K.; Karabiyik, M.; Kaya, S.; Pala, N. *Opt. Express* **2016**, *24*, 13665.

(31)   Cortés, E. *Adv. Opt. Mater.* **2017**, *5*, 1700191.

(32)   Gennaro, S. D.; Sonnefraud, Y.; Verellen, N.; Van Dorpe, P.; Moshchalkov, V. V; Maier, S. A.; Oulton, R. F. *Nat. Commun.* **2014**, *5*, 3748.

(33)   Yorulmaz, M.; Nizzero, S.; Hoggard, A.; Wang, L.-Y.; Cai, Y.-Y.; Su, M.-N.; Chang, W.-S.; Link, S. *Nano Lett.* **2015**, *15*, 3041–3047.

(34)   Yorulmaz, M.; Hoggard, A.; Zhao, H.; Wen, F.; Chang, W.-S. S.; Halas, N. J.; Nordlander, P.; Link, S. *Nano Lett.* **2016**, *16*, 6497–6503.

(35)   Fang, Z.; Wang, Y.; Liu, Z.; Schlather, A.; Ajayan, P. M. *ACS Nano* **2012**, *6*, 10222–10228.

(36)   Joplin, A.; Chang, W.-S.; Link, S. *Langmuir* **2018**, *34*, 3775–3786.

(37)   Yankovich, A. B.; Verre, R.; Olsén, E.; Persson, A. E. O. O.; Trinh, V.; Dovner, G.; Käll, M.; Olsson, E. *ACS Nano* **2017**, *11*, 4265–4274.

(38)   Alonso-Gonzalez, P.; Schnell, M.; Sarriugarte, P.; Sobhani, H.; Wu, C.; Arju, N.; Khanikaev, A.; Golmar, F.; Albella, P.; Arzubiaga, L.; Casanova, F.; Hueso, L. E.; Nordlander, P.; Shvets, G.; Hillenbrand, R. *Nano Lett.* **2011**, *11*, 3922–3926.

(39)   Simoncelli, S.; Li, Y.; Cortés, E.; Maier, S. A. *ACS Nano* **2018**, *12*, 2184–2192.

(40)   Mack, D. L.; Cortés, E.; Giannini, V.; Török, P.; Roschuk, T.; Maier, S. A. *Nat. Commun.* **2017**, *8*, 14513.

(41)   Raab, M.; Vietz, C.; Stefani, F. D.; Acuna, G. P.; Tinnefeld, P. *Nat. Commun.* **2017**, *8*, 13966.

(42)   Fu, B.; Isaacoff, B. P.; Biteen, J. S. *ACS Nano* **2017**, *11*, 8978–8987.

(43)   Wertz, E.; Isaacoff, B. P.; Flynn, J. D.; Biteen, J. S. *Nano Lett.* **2015**, *15*, 2662–2670.

(44)   Biteen, J.; Willets, K. A. *Chem. Rev.* **2017**, *117*, 7241–7243.

(45)   Goodman, A. M.; Hogan, N. J.; Gottheim, S.; Li, C.; Clare, S. E.; Halas, N. J. *ACS Nano* **2017**, *11*, 171–179.

(46)   Jain, P. K.; Qian, W.; El-Sayed, M. A. *J. Am. Chem. Soc.* **2006**, *128*, 2426–2433.

(47)   Cortés, E.; Xie, W.; Cambiasso, J.; Jermyn, A. S.; Sundararaman, R.; Narang, P.; Schlücker, S.; Maier, S. A. *Nat. Commun.* **2017**, *8*, 14880.

(48)   Nakaya, M.; Shikishima, M.; Shibuta, M.; Hirata, N.; Eguchi, T.; Nakajima, A. *ACS Nano* **2012**, *6*, 8728–8734.

(49)   Correa-Puerta, J.; Del Campo, V.; Henríquez, R.; Esaulov, V. A.; Hamoudi, H.; Flores, M.; Häberle, P. *Langmuir* **2017**, *33*, 12056–12064.

(50)   Hobbs, R. G.; Putnam, W. P.; Fallahi, A.; Yang, Y.; Kärtner, F. X.; Berggren, K. K. *Nano Lett.* **2017**, *17*, 6069–6076.
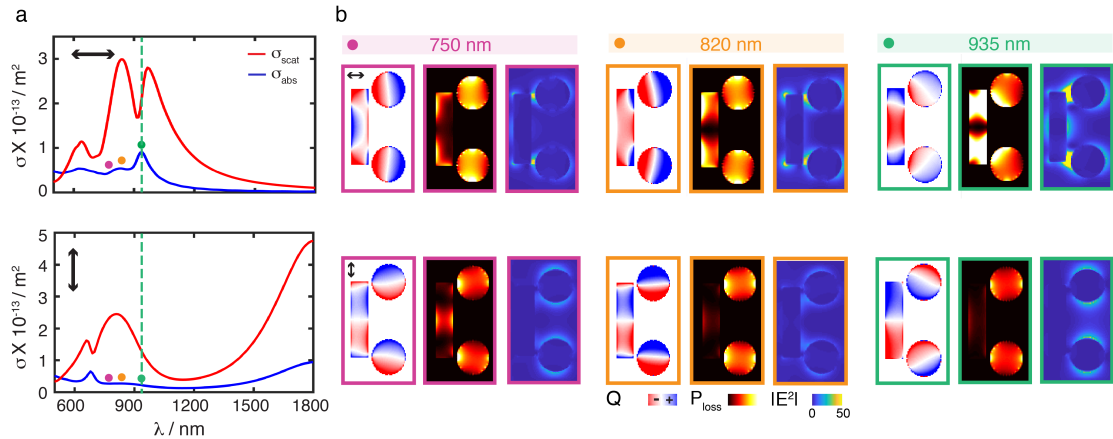
Figures
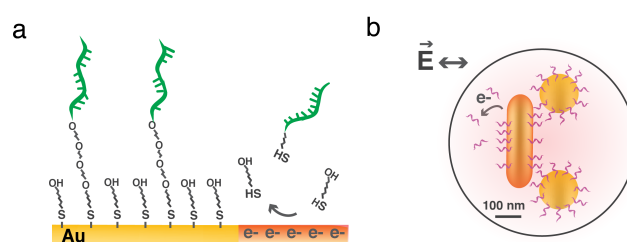
Figure 1. Hot-electron driven Au-S desorption. a, Plasmon resonant femtosecond pulsed-illumination enables cleavage of gold-thiol bonds from the surfaces of gold nanostructures. This photo-release process is induced by hot-electron excitation. **b**, Illustration of the near field coupling between the elements of a multi-resonant

dolmen-type gold nanoantenna. Resonant far field excitation of the two disks induces near field excitation of the bar-shaped particle in the structure leading to the region-selective plasmon-driven reactions.
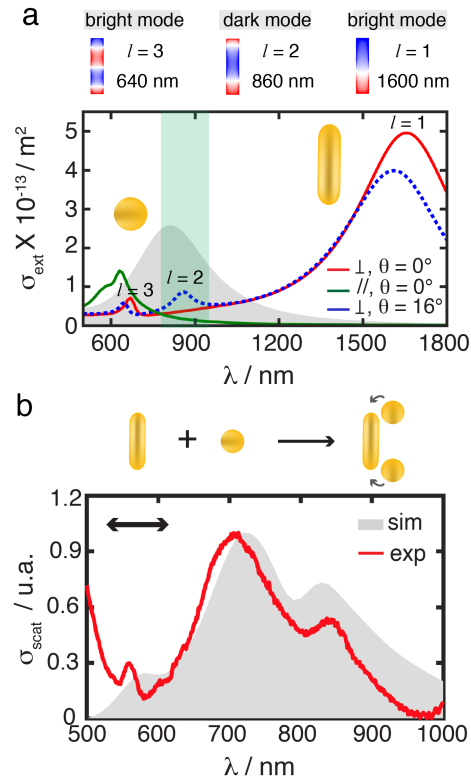

Figure 2. Bright-dark mode hybridization. **a,** Extinction cross sections calculated by FDTD for a single 340×85 nm² nano-sized bar in water at normal incidence angle ($\theta = 0°$) for parallel (green full line) and perpendicular polarization (red full line), as well as, for a perpendicular polarized plane wave with an injection angle of $\theta = 16°$ (blue dashed line). Parallel polarization corresponds to the electrical field polarized along the gap direction in the Fano structure. The calculated charge density distributions for the different order modes ($l = 1$, 2 and 3) are shown in the top. The dashed grey area represents the calculated extinction cross section of a nano-sized disk with a diameter of 160 nm, which presents a dipolar mode close to the $l = 2$ dark resonance of the nano-sized bar. **b,** FDTD-simulated (grey area) and measured (red line) single-antenna scattering spectra of the Fano structure composed of two 160 nm in diameter disks close to a 340×80 nm² bar in air for parallel polarized illumination. The gap size between the bar and the disks is 20 nm.

Figure 3. **Plasmonic response of the Fano structure. a,** Scattering (red line) and absorption (blue line) cross-sections calculated by FDTD for a single gold Fano structure of dimensions 340×80 nm^2 (bar), 160 nm (disks) and gap of 20 nm for parallel (top) and perpendicular (bottom) polarized illumination in water. Green dashed lines and dots highlight the Fano resonance at 935 nm. The violet and orange dots highlights two different wavelengths used in desorption experiments, 750 nm and 820 nm, respectively. **b,** FDTD-calculated charge density (*left*), Q, resistive losses (*middle*), P_{loss}, and electric-field intensity (*right*), E^2, distribution of a single Fano antenna illuminated in water at 750 nm, 820 nm and at the Fano resonance (935 nm) for parallel (top) and perpendicular (bottom) polarized illumination.
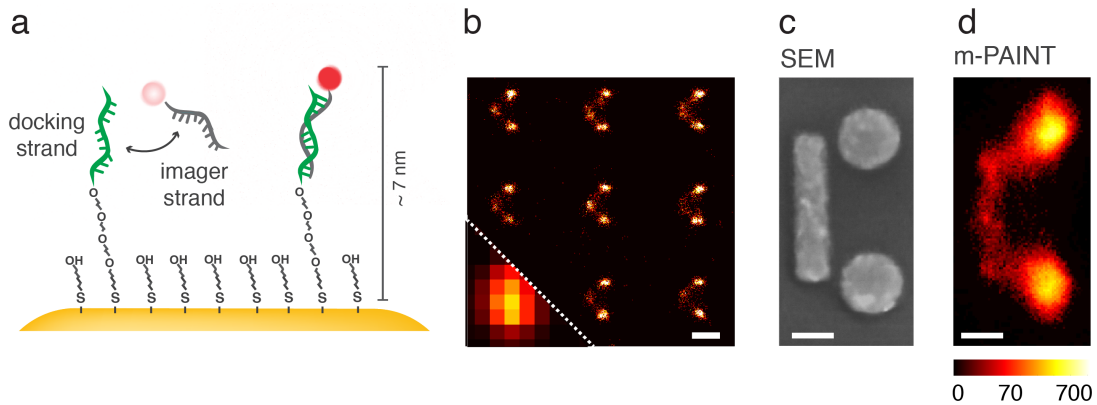
Figure 4. Metallic DNA-PAINT super-resolution imaging technique of plasmonic Fano antennas. a, Schematic representation of the super-resolution metallic DNA-PAINT imaging technique adapted for imaging targets docked to metallic surfaces through a gold-thiol bond. The transient binding of labeled DNA ('imager') strands to their complementary sequence ('docking') strand is detected as a switching between a dark (unbound) and a bright (bound) state. **b,** Diffraction-limited (left bottom corner) and super-resolved m-PAINT image of individual gold Fano nanostructures of dimensions 340×80 nm^2 (bar), 160 nm (disks) and gap of 20 nm. The scale bar corresponds to 300 nm. **c**, SEM image and **d**, average super-resolved m-PAINT image of 36 individual gold Fano structures. The mean number of localizations in individual images is $6{,}500 \pm 1{,}600$. Fluorescence excitation was performed with a linearly polarized 647 nm laser polarized along the longer axis of the nano-sized bar. The scale bar corresponds to 100 nm.
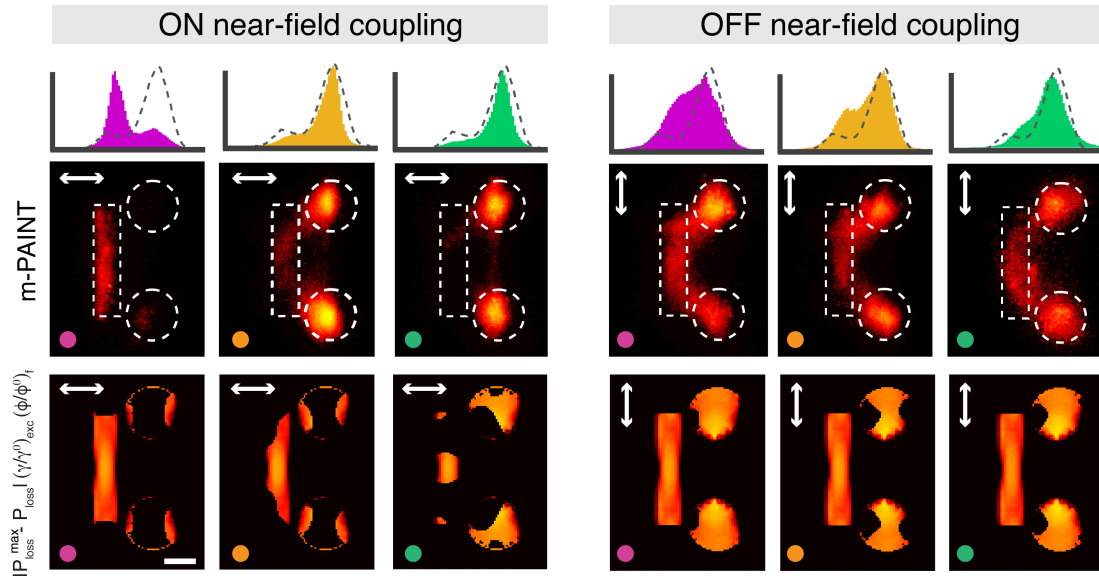
Figure 5. Super-resolved absorption density mapping. *Top*: Normalized histograms of the transverse cross-sectional area of the average super-resolved m-PAINT images displayed in the middle. Dashed grey lines correspond to the normalized control histogram (*i.e.* non-irradiated m-PAINT image, from Figure 4d). *Middle*: Average super-resolved m-PAINT images of 32 to 35 individual gold Fano nanostructures of dimensions 340×80 nm^2 (bar),160 nm (disks) and gap of 20 nm after irradiation with a 750 nm (violet), 820 nm (orange) and 935 nm (green, Fano resonance) linearly polarized femtosecond pulsed laser of 1.9 mJ/cm^2 (750 nm) and 2.6 mJ/cm^2 (820 and 935 nm) fluence. The mean number of localizations in individual images from left to right is $2,100 \pm 500$; $5,800 \pm 1,200$; $4,100 \pm 1,100$; $6,000 \pm 1500$; $4,700 \pm 1,800$ and $5,600 \pm 1,700$. Fluorescence excitation was performed with a linearly polarized 647 nm laser polarized along the longer axis of the nano-sized bar. The power density of the imaging laser (647 nm, CW) is 7 orders of magnitude lower than the peak power of the fs irradiation laser. *Bottom*: FDTD-calculated absorption map distribution considering both resistive losses and dye-antenna coupling effect calculated as detailed in Figure S5 for a single Fano antenna illuminated in water at 750 nm (violet), 820 nm (orange) and 935 nm (green, Fano resonance). White arrows represent the polarization of the incident light. The scale bar corresponds to 100 nm.
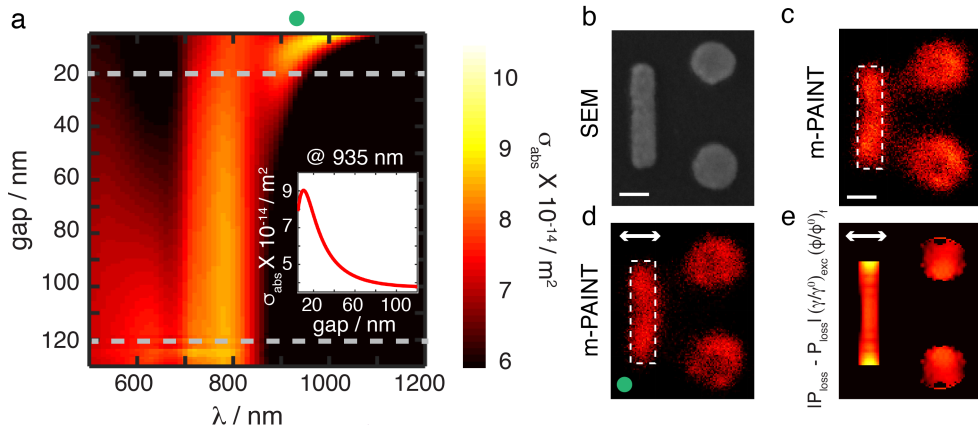
Figure 6. **Breaking plasmon hybridization in Fano structures. a**, Numerical calculation of absorption cross-sections for a single gold Fano structure of dimensions 340×80 nm^2 (bar) and 160 nm (disks) in water for parallel polarized illumination as function of the gap size between the bar and the disks. *Inset*: Absorption cross-section at 935 nm as function of the gap size. The dashed grey lines correspond to the gap sizes of the two structures used in this work, gap of 20 and 120 nm. **b**, SEM image and **c-d**, average super-resolved m-PAINT image of 36 individual gold uncoupled Fano structures (gap = 120 nm) before (**c**) and after (**d**) irradiation with a 935 nm parallel polarized femtosecond pulsed laser of 2.6 mJ/cm^2 fluence. The mean number of localizations for each image are $1{,}100 \pm 400$ and $1{,}000 \pm 400$, respectively. **e**, FDTD-calculated absorption map distribution considering both resistive losses and dye-antenna coupling effect - calculated as detailed in Figure S5 - for a single uncoupled Fano antenna illuminated in water at 935 nm. White arrows represent the polarization of the fs incident light. Fluorescence excitation was performed with a linearly polarized 647 nm laser. The scale bars correspond to 100 nm.

Graphical Table of Contents (TOC)